



HAL
open science

Igneous rock powder identification using colour cameras: A powerful method for space exploration

Frédéric Foucher, N. Bost, G. Guimbretière, A. Courtois, K. Hickman-Lewis,
E. Marceau, P. Martin, Frances Westall

► To cite this version:

Frédéric Foucher, N. Bost, G. Guimbretière, A. Courtois, K. Hickman-Lewis, et al.. Igneous rock powder identification using colour cameras: A powerful method for space exploration. *Icarus*, 2022, 375, pp.114848. 10.1016/j.icarus.2021.114848 . hal-03526397

HAL Id: hal-03526397

<https://hal.science/hal-03526397>

Submitted on 14 Jan 2022

HAL is a multi-disciplinary open access archive for the deposit and dissemination of scientific research documents, whether they are published or not. The documents may come from teaching and research institutions in France or abroad, or from public or private research centers.

L'archive ouverte pluridisciplinaire **HAL**, est destinée au dépôt et à la diffusion de documents scientifiques de niveau recherche, publiés ou non, émanant des établissements d'enseignement et de recherche français ou étrangers, des laboratoires publics ou privés.



Distributed under a Creative Commons Attribution - NonCommercial - NoDerivatives 4.0
International License



Research Paper

Igneous rock powder identification using colour cameras: A powerful method for space exploration

F. Foucher^{a,*}, N. Bost^a, G. Guimbretière^b, A. Courtois^{a,c}, K. Hickman-Lewis^d, E. Marceau^{a,c}, P. Martin^e, F. Westall^a

^a CNRS, Centre de Biophysique Moléculaire, UPR4301, 3E avenue de la Recherche Scientifique, 45071 Orléans Cedex 2, France

^b CNRS, Laboratoire de l'Atmosphère et des Cyclones, UMR8105, 15 avenue René Cassin, 97744 Saint-Denis Cedex 9, La Réunion, France

^c Université d'Orléans, Château de la Source, avenue du Parc Floral, BP 6749, 45067 Orléans Cedex 2, France

^d Department of Earth Sciences, The Natural History Museum, Cromwell Rd, South Kensington, London SW7 5BD, United Kingdom

^e CNRS, Laboratoire de Physique et de Chimie de l'Environnement et de l'Espace, UMR73028, 3E avenue de la Recherche Scientifique, 45071 Orléans Cedex 2, France



ARTICLE INFO

Keywords:

Mars
Rocks
Petrology
Camera
Powder

ABSTRACT

Powdered rocks are commonly present at the surface of extraterrestrial bodies and are widely analysed by in situ space probes. Moreover, a number of rovers exploring the surface of Mars are equipped with drills enabling them to access unaltered material and collect samples. During drilling operations, a cone of powder made of the drilled materials forms at the surface. These powders will be particularly large during the ESA/Roscosmos ExoMars 2022 mission since the rover *Rosalind Franklin* will drill to 2 m depth below the Martian surface. These fines are generally observed by the rovers' cameras after the drilling process and analysed by a limited range of instruments. In order to maximise the scientific return of planetary missions to Mars and other bodies in the solar system, we propose to use the images taken by rover cameras to identify the composition of the powdered materials. This could be particularly useful during the ExoMars 2022 mission where the CLUPI camera will take pictures during drilling and could thus document changes in the regolith composition (Josset et al., 2017). In the absence of a controlled light source, we used an image processing method called CaliPhoto that we previously developed for generic purposes. To test the ability of the method to identify volcanic rocks, more than twenty Mars-analogue samples were crushed at various grain sizes and photographed. The images were then processed via the CaliPhoto method and used to construct a database of reference images. New images were then taken under different lighting conditions, processed using the same method, and compared to the database. We show that it is possible to estimate igneous rock powder lithology with greater than 90% accuracy considering the uncertainties. Furthermore, when using images of polished and powdered samples, identification reaches 100%. We also show that the method permits precise lithological identification of samples that are not in the initial database. Finally, we demonstrate that the proposed method is extremely efficient, while at the same time very easy to implement on any in situ space probe. It could thus be used to help in identifying powdered igneous rocks during future missions to Mars or other rocky body in the solar system.

1. Introduction

Powdery and dusty materials are very common throughout the solar system. For example, asteroids, comets and the Moon are covered by a layer of dust and regolith (Hazeli et al., 2018; Turkevich, 1973). Clays and silicate-rich dusty materials also cover the surface of Mars (e.g., Horgan et al., 2020; Quantin-Nataf et al., 2021). Remote petrological analyses of extra-terrestrial bodies, whether carried out from the Earth or using satellites, are thus mostly representative of these dusty

materials. Powdery materials have also been widely observed during in situ exploration (Goetz et al., 2010; Bish et al., 2013; Blake et al., 2013; Grott et al., 2019). Rovers and landers are generally equipped with tools for removing dust from rocks or grinding their surfaces in order to access the "unaltered" material beneath. The NASA rovers *Spirit* and *Opportunity* were equipped with a RAT (Rock Abrasion Tool) (Squyres et al., 2004) and the *Curiosity* rover with a DRT (Dust Removal Tool) (Grotzinger et al., 2012). The laser of the ChemCam instrument on-board *Curiosity* is also used to remove dust from rock surfaces prior to

* Corresponding author.

E-mail address: frederic.foucher@cnrs.fr (F. Foucher).

<https://doi.org/10.1016/j.icarus.2021.114848>

Received 24 March 2021; Received in revised form 3 December 2021; Accepted 6 December 2021

Available online 13 December 2021

0019-1035/© 2021 The Authors.

Published by Elsevier Inc.

This is an open access article under the CC BY-NC-ND license

(<http://creativecommons.org/licenses/by-nc-nd/4.0/>).

analysis (Grotzinger et al., 2012; Meslin et al., 2013). Similarly, drills are commonly used to obtain samples from below the surface. The *Curiosity* rover made several tens of drill campaigns at the surface of Mars (Abbey et al., 2019, 2020). The *Perseverance* rover of the NASA Mars 2020 mission will also drill to take small cores from the surface (6 cm long and 1.3 cm diameter) to be returned to Earth for further analyses (Farley et al., 2020). Finally, the ESA/Roscosmos ExoMars 2022 rover *Rosalind Franklin* is equipped with a drill capable of reaching a depth of 2 m and of sampling small cores (3 cm long and 1 cm diameter) (Vago et al., 2017).

During drilling phases, a pile of rock powder forms at the surface around the hole (see Fig. 1). On Mars, these fines are of particular interest since they provide access to non-oxidised materials; the powder appears grey whereas the rock surface is reddish (Abbey et al., 2019, 2020). During the ExoMars investigation, the amount of powder will be particularly large since the drill will penetrate down to 2 m depth and the hole will be 3 cm in diameter. The equivalent volume of such a hole is 1400 cm³ (1.4 L) and, due to the expansion, the volume of fines exposed at the surface could be even greater since, except for very porous material, the volume of a solid sample generally increases after powdering. Unfortunately, in the absence of a sampling device other than the drill, these powders cannot be analysed by the ExoMars analytical laboratory, only by its external instruments. Moreover, the PanCam (*Panoramic Camera*) and ISEM (*Infrared Spectrometer for ExoMars*) systems will observe and analyse the fines only after sampling operations have been conducted, since the drill box obscures their field of view during the drilling process (Vago et al., 2017). Also, a part of the fines will inevitably fall back into the hole after the removal of the drill. CLUPI (*Close-Up Imager*) is thus the only instrument able to observe this material during drilling (Josset et al., 2017). Such observations are interesting since, depending on the encountered stratigraphy, the composition of the fines may change during drilling. Indeed, due to the relatively small diameter of the drill it is very unlikely that different rocks will be drilled at the same time. The fines arriving at the surface are thus expected to be representative of a unique layer, except at the interface between two layers. Images of the dome forming at the surface during the drilling should thus differentiate the drilled layers.

On Earth, geological observations or investigations carried out using various geochemical methods are generally made before crushing. Therefore the petrography of solid rock is already known and powders are rarely used for their identification. Furthermore, the crushing process is generally considered to be detrimental since it entails a loss of sample integrity, structure and texture. Crushed rocks are thus only used for specific measurements, such as ICP/AES-MS (Inductively Coupled Plasma/Atomic Emission Spectroscopy-Mass Spectroscopy) for elemental composition or X-Ray Diffraction (XRD) for mineralogy.

On the other hand, sample preparation on-board space probes is generally limited and crushing is an effective method to standardize the amount of sample to be analysed. Thus, during the MSL and ExoMars 2022 missions, the drill cores are crushed prior analysis.

Cameras are among the most common instruments on in situ space probes and photography represents key data during planetary exploration. In order to improve their ability to identify rocks and minerals, in particular for powdered materials, some cameras are equipped with several filters for multispectral imaging, such as Mastcam onboard MSL (Johnson et al., 2016; Wellington et al., 2017) and PanCam WAC onboard ExoMars 2022 (Coates et al., 2017; Cousins et al., 2012). This approach consists in using several photographs of the same field of view taken with different filters in order to obtain reflectance spectra (about 12 points per spectrum).

Here we investigate the extent to which geological information can be deduced from the observation of rock powders (in this case, of igneous materials) using only standard colour cameras, i.e., not equipped with any filter. Since most space missions include cameras, understanding their full capabilities for geological investigations is thus advantageous for maximising their science output during any mission

conducting in situ exploration of the shallow sub-surface of an extra-terrestrial body.

In geosciences, colour photography has been used before to estimate the composition of rocks (Kempe, 2014) and to study their ageing (Iiango et al., 2013; Oestmo, 2013). The Munsell soil colour chart is also commonly used in pedology. Nevertheless, the apparent colour of material is directly dependant on light conditions (hue and intensity) and on the photon detectors; the human eye is limited and person-dependant (e.g., colour blindness) and camera detectors have different colour responses. Precise colour measurement is thus made using UV-Vis spectroscopy (Adams and Filice, 1967) or, if based on photography, requires calibrated cameras and the use of specific light sources (CIE Standard Illuminants D50 or D65 for example) (McCamy et al., 1976).

Recently, we developed a new method, CaliPhoto, in which a reference target is placed around the material to study, in the field of view of the camera. Then, using specific image processing, the target is used to compensate the light conditions (orientation, hue, intensity) and the characteristics of the camera. The RGB values of the material are thus extracted from this processed image and compared with those of other materials potentially taken under different light conditions and/or with different cameras. This method can be used to compare materials, and also to determine specific physical properties and follow their changes with time or environmental conditions (temperature, pH, etc.). The method works well, even in relatively bad lightening conditions. A detailed description the method and of various validation tests can be found in Foucher et al. (2019).

The method has applications in many domains such as:

- construction, to check the homogeneity of optical aspects of materials over large areas or on different faces of a structure, to monitor the ageing of materials over space and time, or to control the water content of cement,
- biology, to pre-identify microbial colonies or, for example, to evaluate their reaction to external stresses,
- material science, to monitor changes during specific experiments,
- cosmetics and dermatology, to assist in the selection of makeup adapted to specific types of skin or to control Sun exposure and prevent sunburn.

Nevertheless, it was initially invented for geological purposes, to compare samples observed in different locations in the field, and for space exploration. Indeed, since cameras are among the most common instruments on-board in situ space probes, the possibility to analyse materials by simply adding a dedicated reference target would constitute an important added value for planetary exploration.

In this study, we focus on the use of the CaliPhoto method for geological applications. In particular, we use Mars-analogue igneous rocks to demonstrate that it is possible to identify (igneous) rock powders and/or estimate their composition from a colour photograph alone with a very good accuracy (higher than 90%). Since the albedo of powders increases with decreasing grain size (Adams and Filice, 1967), we also consider the effect of grain size distribution on the validity of the method. Finally, we apply the method on combined images of polished and powdered samples and demonstrate, using a database of 23 samples, that correct lithological identification of the rock with this method is close to 100%.

2. Materials and methods

2.1. The CaliPhoto method

The CaliPhoto method (Fig. 2) was developed in order to be able to

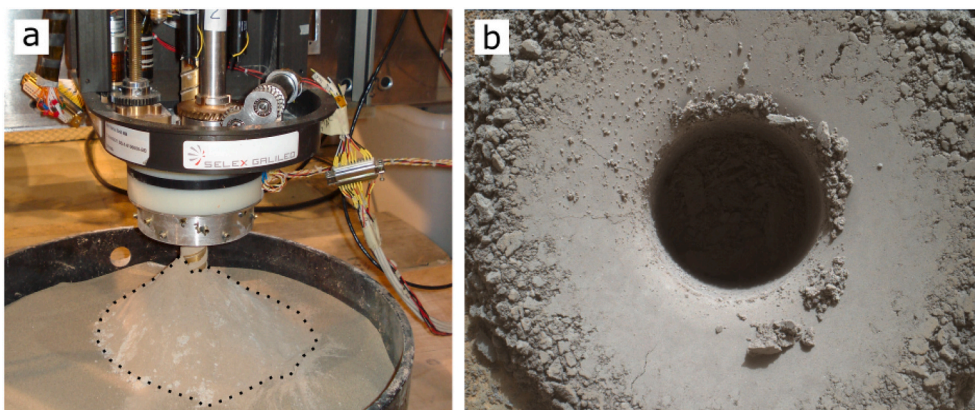


Fig. 1. (a) Formation of a cone of fines during a simulated ExoMars 2022 drilling phase (Credit ESA/Thales Alenia Space - Italia & SELEX Galileo). (b) Drill fines from the Oudam site observed by Curiosity's MAHLI camera (MSL, NASA) on mission sol 1361 (Credit NASA/JPL/Malin Space Science Systems). The drill hole is 1.6 cm wide.

compare the colour of materials from photographs taken using uncalibrated standard digital colour cameras¹ and under different, uncalibrated lightening conditions (Foucher et al., 2019). The method requires the addition of a reference target consisting of a white 4:3 ratio rectangle, surrounded by 24 squares of different colours arranged in a rectangle, surrounding another white rectangle (Fig. 2a). The theoretical RGB values of the squares correspond to those of the standard GretagMacBeth ColorChecker values defined to cover a wide range of colours (Pascale, 2016). The centre of the target is cut in order to make a rectangular window through which the sample is viewed and photographed. For colour comparison, a reference photograph of the target is made. All subsequent images are processed according to this photograph with the aim of obtaining similar RGB values for the colour squares. The whole target is used to correct the perspective, the two white rectangles are used to correct the light intensity, hue and orientation, and the colour squares are used to correct the colour. It is essential, though, that the reference target be placed such that the lightening conditions are similar to those of the material to be photographed (ideally in contact).

The main advantage of the CaliPhoto method is that the target can be printed using any colour printer and works with any photographic device (camera, smartphone, scanner, etc.). Indeed, since the image processing is based on a reference photograph, the colour of the squares with respect to their theoretical values is not relevant. On the other hand, as a consequence, the CaliPhoto colour associated with a material after processing may be slightly different from that observed by human eyes under normal sunlight. Nevertheless, it is important to note that the method has not been developed to obtain “visually appealing” colours but to accurately compare the RGB data associated with different materials. Most importantly, this also means that all the measurements have to be made using the same target. The use of a new target requires a supplementary calibration step and/or imply the need to redo all the measurements (Foucher et al., 2019).

Although the method works using any colour camera, for this study we used a “space mission-relevant” colour camera: a Sigma SD15 equipped with a Foveon X3F 2652 × 1768 pixel sensor similar to that of CLUPI, the ExoMars 2022 camera (Josset et al., 2017). Foveon (Sigma) sensors are composed of three layers and determine colour as a function of photon penetration depth, making it very similar in principle to film photography technology.

The colour associated with the material appearing in the centre of the target on the processed images can be defined using different parameters. For relatively homogeneous samples, the easiest approach is to use

the average RGB colour. Materials i and j can then be compared using the following equation (for 8bit RGB colour encoding, i.e., for R, G and B ranging from 0 to 255):

$$\Delta_{ij} = \frac{\sqrt{(R_i - R_j)^2 + (G_i - G_j)^2 + (B_i - B_j)^2}}{\sqrt{255^2 + 255^2 + 255^2}} \quad (1)$$

It is also possible to study the rg chromaticity defined using the (r, g, b) parameters given by:

$$r = \frac{R}{R + G + B}; g = \frac{G}{R + G + B}; b = \frac{B}{R + G + B} \quad (2)$$

Where r , g and b are, respectively, the proportions of red, green and blue. r , g and b range from 0 to 1 and their sum is equal to 1. Another important parameter is the luminance defined (for 8bit encoding) as follows:

$$\mu = \frac{R + G + B}{3 \cdot 255} \quad (3)$$

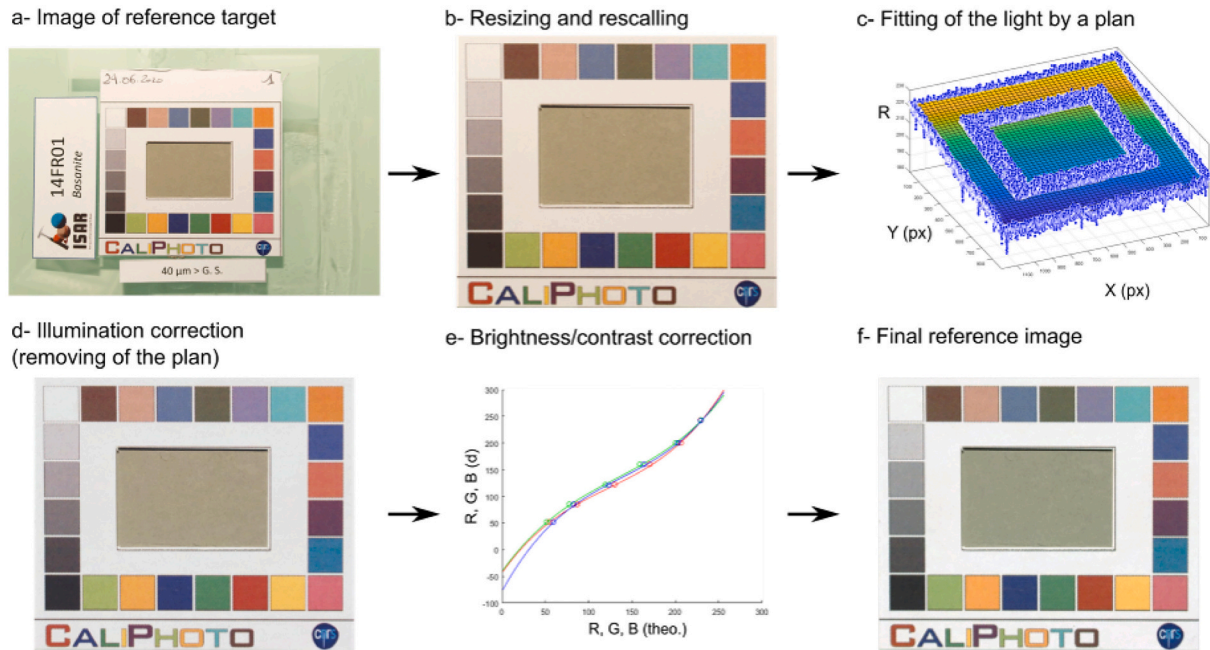
2.2. Analogue rocks

The majority of rocks at the surface of Mars is volcanic in origin (e.g., McSween et al., 2009). Consequently, this study focuses on the use of the CaliPhoto method to identify drilled unaltered volcanic rocks from their fines. We collected various rocks from the Massif Central, France, plus one sample of obsidian from Mono Lake, California, USA, in order to cover a large range of volcanic rock types, as designated in the compositional Total Alkali Silica (TAS) diagram (McSween et al., 2009). We also used the Mars analogue ESA-01-E, from the European Space Agency Exploration Sample Analogue Collection (ESA²C) (Smith et al., 2018). Samples were analysed by ICP-OES for major elements at the SARM, Nancy, France, in order to obtain their elemental compositions. These analogue samples are available via the *International Space Analogue Rockstore* (ISAR), <http://www.isar.cnrs-orleans.fr> (Bost et al., 2013), while ESA-01-E is housed at The Natural History Museum, London. The detailed list of samples, including their major element compositions, is displayed in Table 1.

To assure mission representativeness, we considered previous observations of powders generated at the surface of Mars. In the MAHLI images of the Curiosity drill sites available on the NASA JPL website it is not possible to visualise individual grains in the fines on the areas flattened by the drilling head (see Fig. 1b). This indicates that the grain size distribution of the powders is, at most, a few tens of μm , according to the resolution of that camera (Abbey et al., 2019, 2020). Similarities in the specifications of the drilling devices used during space missions (speed, applied strain, etc.) and the environmental conditions (e.g., no liquid

¹ In digital photography, an image is made of pixels in which the colour is defined using three values: R, G and B (red, green and blue).

Step 1: creation of a CaliPhoto reference image of the target



Step 2: CaliPhoto image processing of samples

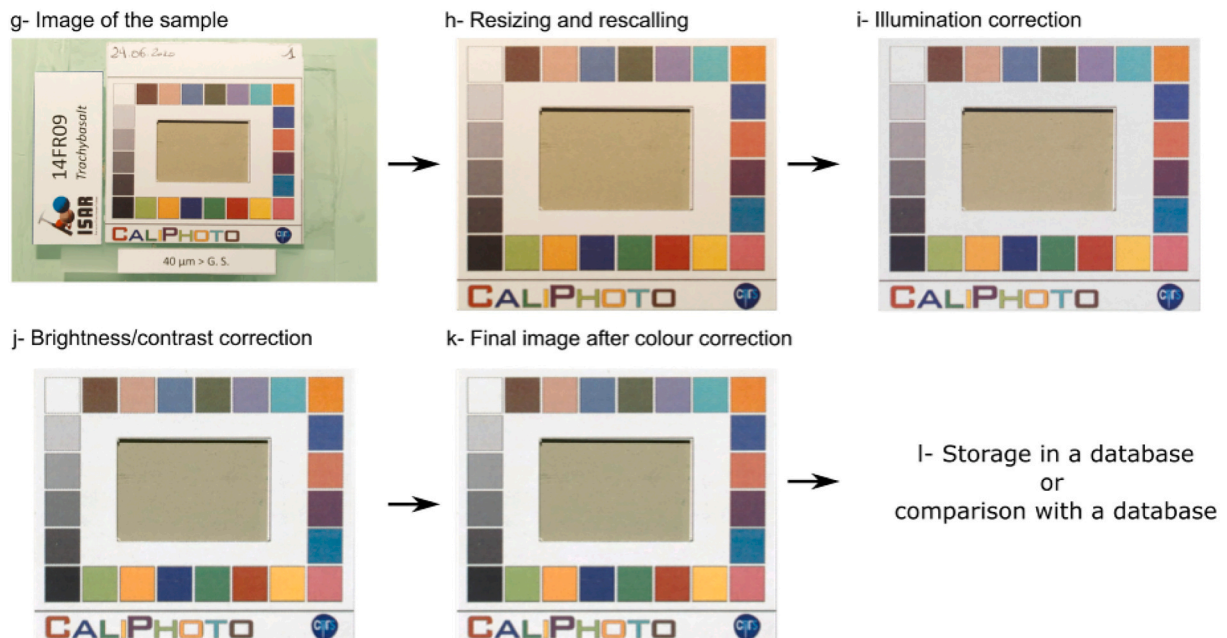


Fig. 2. Principle of the CaliPhoto image processing method. Step 1: creation of a reference image of the target. (a) Any “good” photograph can be used (here a photograph of sample 14FR01 is used). (b) The image is resized to correct for the perspective and rescaled to obtain a 1200×1020 px image. (c) The light plan is calculated using the white rectangles of the target and removed from the image to correct for the orientation of the illumination (d). (e) The greyscale squares are used to improve the brightness and contrast of the image. (f) The final CaliPhoto reference image for the study is obtained. Step 2: CaliPhoto image processing of samples. (g) Raw photograph of the sample. The image processing (h to j) is similar to the previous case but with the addition of a complementary step in which the reference image is used to correct the colours (k). For a known sample, the average RGB and/or colour vector can be stored into a database. Conversely, for an unknown sample, its identification requires comparison of the average RGB and/or colour vector with a database.

water) suggest that the grain size distribution of the fines produced during drilling would be, for most missions, similar to that observed by *Curiosity*. The samples were thus crushed and sieved to obtain powders of a grain size distribution lower than $40 \mu\text{m}$ as a first approximation. Each fragment of rock was crushed in its entirety in order to avoid potentially sorting of the rock minerals according to their hardness. Each

powder was then placed into a rectangular sample holder ($2.5 \times 2 \times 0.2$ cm) surrounded by the CaliPhoto reference target and flattened in order to obtain an homogeneous surface similar to those observed during the MSL mission (Fig. 1b). Powders were illuminated using a halogen lamp and photographed using the Sigma SD15 camera. Finally, the CaliPhoto algorithm was used to process the images of the studied powders as

Table 1
List of analysed samples.

Samples			ICP-OES data (mass %)										
ISAR reference	Type of rock	Locality	SiO ₂	Al ₂ O ₃	Fe ₂ O ₃	MnO	MgO	CaO	Na ₂ O	K ₂ O	<i>Na₂O + K₂O</i>	TiO ₂	P ₂ O ₅
14FR01	Basanite	La Roche Sauterre, Massif Central, France	43.38	12.56	12.67	0.19	12.46	10.73	3.05	1.88	<i>.94</i>	3.18	0.69
14FR02	Trachyandesite	Puy de la Nugère, Massif Central, France	57.43	17.91	6.93	0.22	1.95	4.54	5.56	3.45	<i>9.01</i>	1.17	0.66
14FR03	Basaltic trachyandesite	Puy Pariou, Massif Central, France	53.46	17.38	9.57	0.20	3.08	6.30	4.72	2.53	<i>7.25</i>	1.76	0.93
14FR04	Picrobasalt	Puy Charade, Massif Central, France	41.43	12.75	14.14	0.22	10.52	11.07	2.30	0.49	<i>2.79</i>	3.31	0.71
14FR05	Trachybasalt	Le Grand Suchet, Massif Central, France	48.23	16.47	11.37	0.21	5.20	9.02	3.80	2.04	<i>5.84</i>	2.30	0.72
14FR07	Trachybasalt	Puy de Barme, Massif Central, France	49.13	17.81	10.90	0.22	3.43	7.67	4.22	2.04	<i>6.26</i>	2.29	1.21
14FR08	Tephrite/basanite	Les Granges, Massif Central, France	42.86	14.50	13.62	0.22	7.58	11.02	3.86	1.85	<i>5.71</i>	3.21	0.92
14FR09	Trachybasalt	Cascade du Trador, Massif Central, France	48.75	17.14	8.97	0.21	3.14	8.19	4.07	2.39	<i>6.46</i>	2.34	0.67
14FR11	Trachybasalt	Le Pessy, Massif Central, France	47.38	16.20	11.48	0.18	4.93	9.15	3.83	2.41	<i>6.24</i>	3.09	0.66
14FR12	Rhyolite	Charlannes, Massif Central, France	73.54	14.43	1.54	0.17	0.04	0.33	6.08	4.58	<i>10.66</i>	0.10	0.00
14FR14	Trachybasalt	Roche Vendeix, Massif Central, France	48.34	17.92	8.62	0.19	2.85	8.27	3.89	2.35	<i>6.24</i>	2.36	0.91
14FR17	Trachyte	Roche vendeix, Massif Central, France	62.76	17.25	4.56	0.14	1.05	2.50	4.87	4.90	<i>9.77</i>	0.95	0.35
14FR18	Phonolite	Bozat, Massif Central, France	60.91	18.88	3.05	0.18	0.40	1.43	7.40	6.00	<i>13.39</i>	0.53	0.10
14FR19	Trachyte	Bozat, Massif Central, France	61.76	16.74	5.33	0.15	1.41	3.36	5.00	4.52	<i>9.53</i>	1.15	0.38
14FR21	Trachyandesite	Puy de Mareilh, Massif Central, France	54.91	16.65	8.28	0.16	3.61	6.78	4.72	3.55	<i>8.27</i>	2.05	0.60
14FR22	Trachyte	Puy de Mareilh, Massif Central, France	64.51	15.95	4.02	0.10	1.43	2.78	5.03	4.98	<i>10.01</i>	0.88	0.22
14FR23	Basanite	La Banne d'Ordanche, Massif Central, France	43.39	14.38	13.66	0.19	8.63	11.51	3.30	1.52	<i>4.82</i>	3.20	0.64
14FR24	Picrobasalt	La Banne d'Ordanche, Massif Central, France	41.20	14.65	13.94	0.20	8.77	11.20	2.23	0.65	<i>2.88</i>	3.24	0.68
14FR25	Basalt	La Banne d'Ordanche, Massif Central, France	45.21	17.42	11.20	0.20	5.04	8.66	2.08	2.88	<i>4.97</i>	2.84	0.91
14FR26	Rhyolite	La Banne d'Ordanche, Massif Central, France	76.18	13.52	1.18	0.06	0.04	0.26	4.67	4.83	<i>9.50</i>	0.16	0.00
14FR27	Trachyte	Roche Tuilière, Massif Central, France	61.29	19.80	2.20	0.13	0.19	0.89	5.99	6.30	<i>12.29</i>	0.31	0.00
12US02	Obsidian	Mono Lake, California, USA	75.89	12.35	1.21	0.05	0.03	0.58	3.97	4.60	<i>8.57</i>	0.06	0.00
ESA-01-E	Picrobasalt	Craig's Quarry, County Antrim, Northern Ireland	44.18	16.03	14.46	0.19	7.71	8.72	2.75	0.18	<i>2.93</i>	1.66	0.16

ICP-OES data giving the composition (major elements in mass %). We used italics for this specific column because it corresponds to the sum of the two previous ones. This sum is used to plot the TAS digram (Fig. 8).

displayed in Fig. 3 (original images are given in Fig. S1). The colours of the powders are various greenish/yellowish shades of grey.

3. Results

3.1. Identification of rock powder from a reference database

In order to test the identification of rock powder using the CaliPhoto method, the average RGB values of the powders were extracted from the images displayed in Fig. 3 in order to constitute a reference database. Each powder was then mixed and new images were taken under different illumination conditions (i.e., a change in the camera position and on the orientation and intensity of the light source). These new images of the samples, for which the names start by “UNK-”, are then considered as images of “unknown” samples that need to be identified by comparison with those of the database. They are displayed in Figs. S1 and S2 before and after CaliPhoto image processing, respectively. The average RGB values of the “unknown” powders were compared to those of the database using a matching parameter defined by:

$$M_{ij} = 1 - \Delta_{ij} \quad (4)$$

where Δ_{ij} is the difference in colour defined by Eq. (1). Examples of matching results are displayed in Table 2 (full results can be found in Table S1). For 50% of powders, the identification is exact, i.e., the studied powder corresponds to the highest matching identification from the database. In 77% of cases, the studied powder is in the top two matches, and in 95% of cases, it is in the top three. Moreover, when the studied powder is not in the first position, the difference with the best match is always lower than 1% except for two samples (14FR08, 1.54%, and 14FR12, 1.56%).

The uncertainty in the powder colour, estimated from the differences in the RGB values of the colour squares of the target on the corrected images, is of about 1%. Considering this 1% uncertainty, it is possible to state that the identification is correct for about 91% of the samples. More interestingly, for 82% of cases, the best match is a rock with a similar or adjacent composition as defined by the TAS diagram (e.g., picrobasalt and basalt or trachyandesite and basaltic trachyandesite).

3.2. Identification of unknown rocks

The aim of this study is to evaluate the ability of the CaliPhoto method to identify the composition of unknown powdered igneous rocks

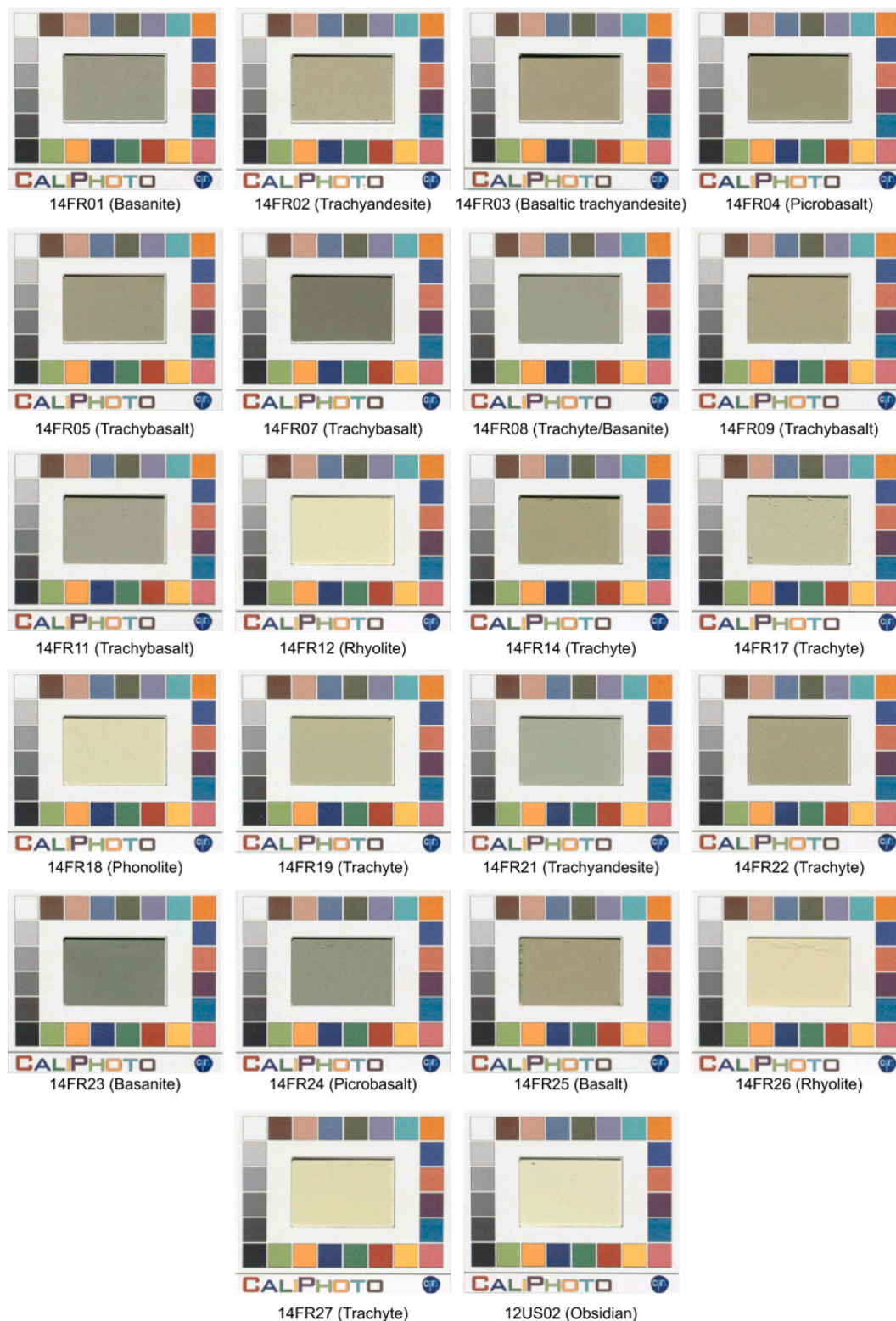


Fig. 3. Images of the studied rock powders (grain size < 40 μm) after CaliPhoto image processing. Image size 57 × 78 mm (1200 × 1020 px).

on Mars. During space exploration, the observed powder will be unknown and thus not included in the reference database. The Mars analogue rock ESA-01-E, chosen by ESA for its physical and chemical similarities to known Martian basalts (Martin and Duvet, 2019; Smith et al., 2018), was used to test the ability of the CaliPhoto method to estimate the composition of an unknown powder. The sample was crushed and sieved to obtain powders with a grain size distribution

lower than 40 μm and its average RGB value after image processing was compared to those of the reference database. Raw and processed images are displayed in Fig. 4. The ICP-OES analysis displayed in Table 1 shows that ESA-01-E sample is a picrobasalt.

The RGB matching percentages, given by Eq. (4), against the samples of the reference database are given in Table 3. The best match occurs with samples 14FR24 and 14FR04 at 97.99% and 97.95%, respectively,

Table 2
Example of matching between the average RGB values of four powders and those of the reference sample database.

		UNK-14FR01			UNK-14FR02			UNK-14FR03			UNK-14FR04
Database		Basanite	Database		Trachyandesite	Database		Basaltic trachyandesite	Database		Picrobasalt
14FR24	Picrobasalt	98,75%	14FR02	Trachyandesite	98,53%	14FR25	Basalt	99,19%	14FR04	Picrobasalt	98,34%
14FR04	Picrobasalt	98,72%	14FR09	Trachybasalt	98,27%	14FR03	Basaltic trachyandesite	99,10%	14FR24	Picrobasalt	97,74%
14FR01	Basanite	98,40%	14FR11	Trachybasalt	97,50%	14FR05	Trachybasalt	98,54%	14FR05	Trachybasalt	96,98%
14FR05	Trachybasalt	98,24%	14FR22	Trachyte	97,10%	14FR14	Trachybasalt	98,13%	14FR01	Basanite	96,66%
14FR08	Tephrite/basanite	96,78%	14FR21	Trachyandesite	96,82%	14FR04	Picrobasalt	98,04%	14FR25	Basalt	96,07%
14FR25	Basalt	96,76%	14FR14	Trachybasalt	96,35%	14FR22	Trachyte	97,61%	14FR03	Basaltic trachyandesite	95,67%
14FR03	Basaltic trachyandesite	96,40%	14FR03	Basaltic trachyandesite	95,70%	14FR01	Basanite	97,58%	14FR08	Tephrite/basanite	95,13%
14FR14	Trachybasalt	95,82%	14FR08	Tephrite/basanite	95,59%	14FR08	Tephrite/basanite	97,19%	14FR14	Trachybasalt	95,03%
14FR22	Trachyte	95,46%	14FR25	Basalt	95,40%	14FR09	Trachybasalt	96,44%	14FR22	Trachyte	94,42%
14FR11	Trachybasalt	94,73%	14FR19	Trachyte	95,16%	14FR11	Trachybasalt	96,02%	14FR11	Trachybasalt	93,26%
14FR09	Trachybasalt	94,21%	14FR05	Trachybasalt	94,37%	14FR24	Picrobasalt	95,85%	14FR09	Trachybasalt	93,19%
14FR23	Basanite	91,71%	14FR01	Basanite	94,15%	14FR02	Trachyandesite	93,34%	14FR23	Basanite	92,51%
14FR02	Trachyandesite	91,26%	14FR04	Picrobasalt	93,17%	14FR21	Trachyandesite	92,41%	14FR02	Trachyandesite	90,08%
14FR21	Trachyandesite	91,11%	14FR24	Picrobasalt	91,58%	14FR19	Trachyte	90,05%	14FR07	Trachybasalt	89,76%
14FR07	Trachybasalt	88,55%	14FR17	Trachyte	91,38%	14FR23	Basanite	89,22%	14FR21	Trachyandesite	89,57%
14FR19	Trachyte	88,08%	14FR23	Basanite	84,41%	14FR07	Trachybasalt	86,41%	14FR19	Trachyte	86,88%
14FR17	Trachyte	84,26%	14FR26	Rhyolite	82,73%	14FR17	Trachyte	86,20%	14FR17	Trachyte	82,99%
14FR26	Rhyolite	75,49%	14FR27	Trachyte	82,21%	14FR26	Rhyolite	77,62%	14FR26	Rhyolite	74,33%
14FR27	Trachyte	75,02%	14FR18	Phonolite	81,93%	14FR27	Trachyte	77,09%	14FR27	Trachyte	73,84%
14FR18	Phonolite	74,79%	14FR07	Trachybasalt	81,35%	14FR18	Phonolite	76,76%	14FR18	Phonolite	73,52%
14FR12	Rhyolite	72,09%	14FR12	Rhyolite	79,28%	14FR12	Rhyolite	74,13%	14FR12	Rhyolite	70,87%
12US02	Obsidian	71,32%	12US02	Obsidian	78,46%	12US02	Obsidian	73,27%	12US02	Obsidian	70,03%

These powders, considered as “unknown”, were imaged after mixing and in different light conditions than those of the database. Results are given in percent match. (Full results are displayed in Supplementary Materials).



Fig. 4. Images of the ESA-01-E analogue sample, polished and powdered (G.S. < 40 μm). (a) Raw images, (b) resized images and (c) final images after CaliPhoto image processing.

both of which are microbasalts. The CaliPhoto method thus successfully identified ESA-01-E as a microbasalt.

3.3. Grain size distribution effects

3.3.1. Effect on luminance

The main difference between the sample powders is their luminance, all powders exhibiting different, more or less yellowish/greenish, shades of grey. Up to this point, the studied powders were compared after sieving to 40 μm, according to observations previously made on Mars. Unfortunately, the decrease of grain size distribution of a powder is associated with an increase in albedo corresponding to an increase of the luminance on the photographs (Adams and Filice, 1967). In order to extend the CaliPhoto method to “natural” unsorted powders, it is relevant to evaluate the influence of grain size distribution on the method. All samples were thus sieved to various grain size distributions (G.S.): 160 μm > G.S. > 100 μm, 100 μm > G.S. > 63 μm, 63 μm > G.S. > 40 μm and 40 μm > G.S. Freshly broken surfaces and polished surfaces were also prepared. A total of 132 samples was thus obtained. The raw and processed images of these samples are displayed in Figs. S1 and S2 respectively. The average colours of these powders, their luminance, and

Table 3

Matching (in percent) of the average RGB values of the ESA-01-E with respect to those of the reference sample database.

Database		ESA-01-E
Picrobasalt		Picrobasalt
14FR24	Picrobasalt	97,99%
14FR04	Picrobasalt	97,95%
14FR05	Trachybasalt	96,67%
14FR01	Basanite	96,56%
14FR25	Basalt	95,66%
14FR03	Basaltic trachyandesite	95,20%
14FR08	Tephrite/basanite	94,99%
14FR14	Trachybasalt	94,69%
14FR22	Trachyte	94,09%
14FR11	Trachybasalt	93,07%
14FR09	Trachybasalt	92,86%
14FR23	Basanite	92,85%
14FR07	Trachybasalt	90,01%
14FR02	Trachyandesite	89,78%
14FR21	Trachyandesite	89,44%
14FR19	Trachyte	86,65%
14FR17	Trachyte	82,76%
14FR26	Rhyolite	74,06%
14FR27	Trachyte	73,60%
14FR18	Phonolite	73,29%
14FR12	Rhyolite	70,63%
12US02	Obsidian	69,80%

The best matching occurs for picrobasalt powders.

Nevertheless, the importance of this effect varies depending on the initial colour of the sample before crushing rather than on its elemental composition. Thus, this effect is particularly strong in the case of obsidian, which is very dark in hand specimen and polished samples and very bright in powdered samples, whereas it is relatively limited for rhyolite, which is bright in both hand sample and powder. Interestingly, the *rg* chromaticity remains relatively constant, with proportions of *r*, *g* and *b* close to 1/3, 1/3, 1/3 (i.e., shades of grey). As a consequence, the colours of the different powders are relatively close and all are shades of grey regardless of the grain size distribution.

3.3.2. Effect on colour distribution

The loss of texture induced by the crushing process is associated with the homogenization of the colour of the rock. This is particularly true for coarse-grained rocks comprising large minerals with various colours, such as trachytes, which are composed of light and dark minerals and form a grey powder after crushing as seen in Fig. 6. This homogenization is all the more important when grain size decreases. In order to evaluate this effect, it is useful to define a vector based on different colour histograms of the image. Here, we merged the histograms of *R*, *G*, *B*, *r*, *g*, *b* and μ into a unique colour vector *Vec* defined for material *i* as follows (for 8bit colour encoding):

$$Vec_i = \frac{Hist(R_i/255) \cup [1 + Hist(G_i/255)] \cup [2 + Hist(B_i/255)] \cup [3 + Hist(r_i)] \cup [4 + Hist(g_i)] \cup [5 + Hist(b_i)] \cup [6 + Hist(\mu_i)]}{Max\{R_i/255, G_i/255, B_i/255, r_i, g_i, b_i, \mu_i\}} \quad (5)$$

their (*r*,*g*,*b*) values are shown in Fig. 5.

An increase in luminance during the crushing process is clearly observed with decreasing grain size, irrespective of sample type.

where *Hist*(*R_i*/255) corresponds to the normalized histogram of *R_i*, rounded to 0.05, over the sample area, [1 + *Hist*(*G_i*/255)] to the

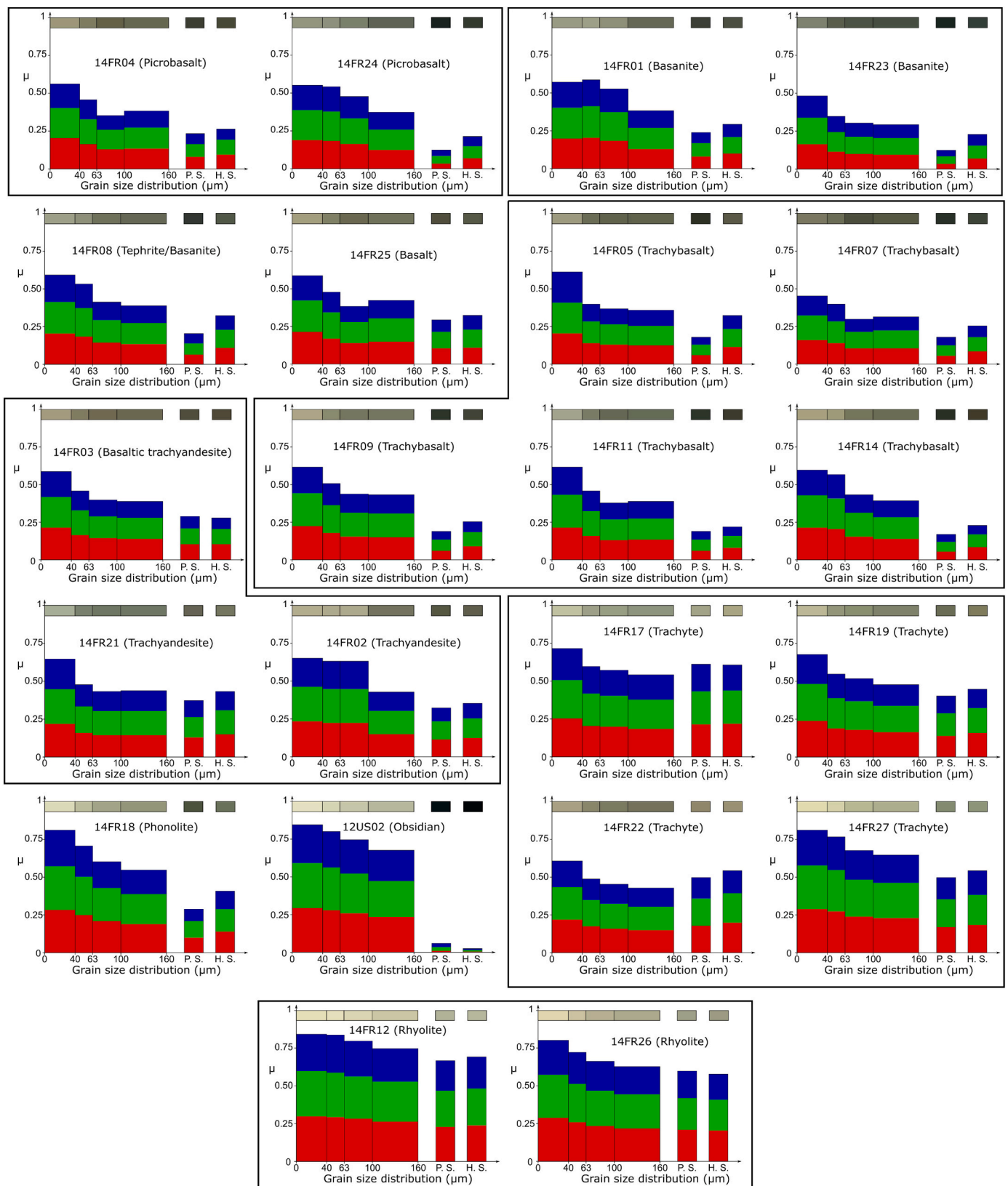


Fig. 5. Luminance versus grain size distribution for the studied reference samples. The RGB contribution to the luminance is reported in each bar. The upper coloured bar indicates the average colour of the powder.

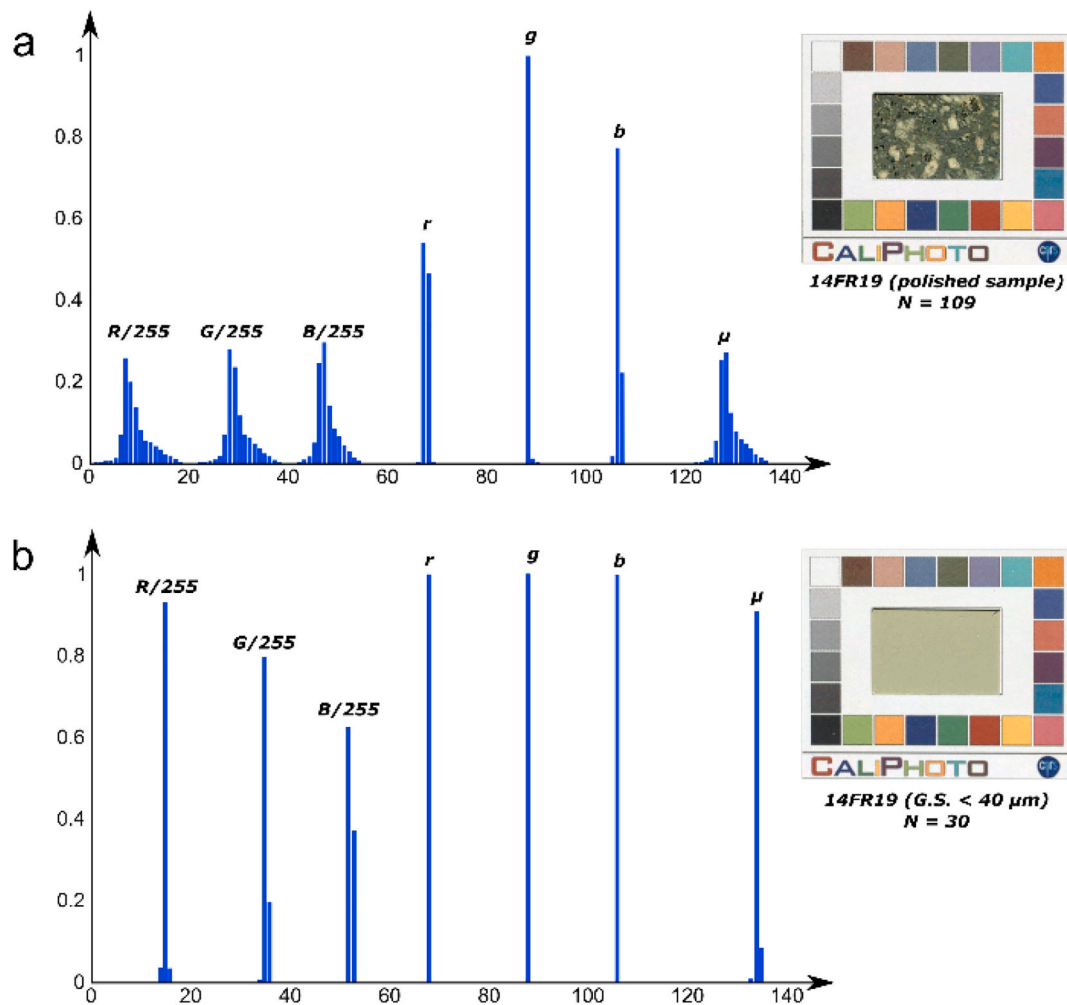


Fig. 6. Colour vector of sample 14FR19 (trachyte), a- polished and b- powdered (G.S. < 40 μm) sample showing that the crushing process is associated with homogenization of the colour (narrowing of the histograms) and with an increase in the luminance μ (shifting of the μ histogram on the right).

normalized histogram of G_i , rounded to 0.05, displayed between 1 and 2, $[2 + Hist(B_i/255)]$ to the normalized histogram of B_i , rounded to 0.05, displayed between 2 and 3, $[3 + Hist(r)]$ to the histogram of r_i , rounded

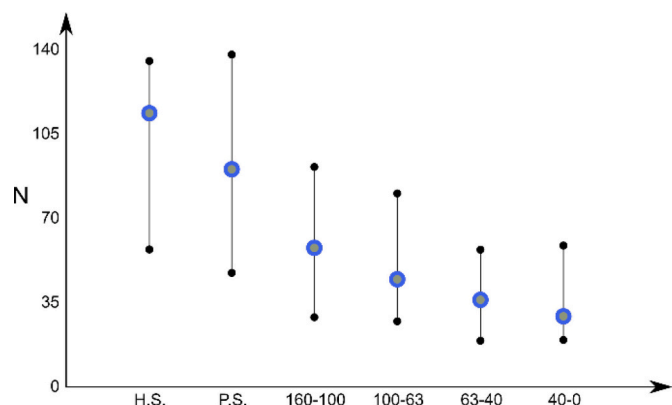


Fig. 7. Average values of the number N of non-null values of colour vectors for the 132 samples versus sample preparation (blue circles): hand sample (H.S.), polished surface (P.S.) and powdered samples of different grain size distributions (160–100 μm, 100–63 μm, 63–40 μm and 40–0 μm). Black lines denote the maximal and minimal values for each sample preparation. (For interpretation of the references to colour in this figure legend, the reader is referred to the web version of this article.)

to 0.05, displayed between 3 and 4, $[4 + Hist(g)]$ to the histogram of g_i , rounded to 0.05, displayed between 4 and 5, $[5 + Hist(b)]$ to the histogram of b_i , rounded to 0.05, displayed between 5 and 6, $[6 + Hist(μ)]$ to the histogram of $μ_i$, rounded to 0.05, displayed between 3 and 4, and $Max\{R_i/255, G_i/255, B_i/255, r_i, g_i, b_i, (μ_i/256)\}$ to the maximal values of the different histograms. Each vector is thus composed of 140 values (see Fig. 6).

Colour distribution is then evaluated using the number N of non-null values of Vec ; the lower is the value, the higher the homogeneity of the powder. The average value of the distribution for the different sample preparations is displayed in Fig. 7. This denotes homogenization of colour with decreasing grain size distribution. The high values obtained for hand samples are explained both by rock texture (i.e., the size and colour of the rock-forming minerals) and by surface roughness forming shadows, whereas the values obtained for polished surfaces are only influenced by the rock texture, explaining the observed decrease in the colour distribution.

3.3.3. Effect on identification

In order to determine if it is possible to identify both the rock and its grain size, vectors associated with the “unknown” powders (G.S. < 40 μm) were compared against vectors of the 132 samples using the following equation:

$$M_{12}^{Vec} = 1 - \frac{\sqrt{(Vec_1 - Vec_2)^2}}{Vec_1 + Vec_2} \quad (6)$$

Table 4

Examples of matching results of the average RGB values in percent for three powders (G.S. < 40 µm) with respect to those of the reference sample database (only the first 30 lines over 132 are shown; see Table S2 in supplementary materials for full results).

Database			UNK-14FR01	Database			UNK-14FR02	Database			UNK-14FR03
			Basanite				Trachyandesite				Basaltic trachyandesite
14FR01	40-0 µm	Basanite	78,91%	14FR02	63-40 µm	Trachyandesite	96,88%	14FR25	40-0 µm	Basalt	94,71%
14FR03	100-63 µm	Basaltic trachyandesite	78,91%	14FR02	100-63 µm	Trachyandesite	89,39%	14FR14	63-40 µm	Trachybasalt	88,82%
14FR05	40-0 µm	Trachybasalt	77,61%	14FR26	160-100 µm	Rhyolite	84,25%	14FR03	40-0 µm	Basaltic trachyandesite	88,43%
14FR18	160-100 µm	Phonolite	76,12%	14FR09	40-0 µm	Trachybasalt	83,65%	14FR05	40-0 µm	Trachybasalt	87,94%
14FR19	63-40 µm	Trachyte	75,80%	14FR02	40-0 µm	Trachyandesite	83,28%	14FR04	40-0 µm	Picrobasalt	87,00%
14FR25	40-0 µm	Basalt	73,86%	14FR27	160-100 µm	Trachyte	79,53%	14FR14	40-0 µm	Trachybasalt	78,39%
14FR04	40-0 µm	Picrobasalt	73,09%	14FR22	40-0 µm	Trachyte	74,78%	14FR22	40-0 µm	Trachyte	74,38%
14FR24	40-0 µm	Picrobasalt	71,60%	14FR18	100-63 µm	Phonolite	73,96%	14FR18	100-63 µm	Phonolite	73,74%
14FR14	63-40 µm	Trachybasalt	71,47%	14FR14	40-0 µm	Trachybasalt	71,93%	14FR01	40-0 µm	Basanite	71,48%
14FR03	40-0 µm	Basaltic trachyandesite	70,20%	14FR26	100-63 µm	Rhyolite	71,67%	14FR03	100-63 µm	Basaltic trachyandesite	71,48%
14FR26	P.S.	Rhyolite	68,99%	14FR11	40-0 µm	Trachybasalt	69,83%	14FR18	160-100 µm	Phonolite	70,16%
14FR01	63-40 µm	Basanite	68,90%	14FR27	100-63 µm	Trachyte	62,74%	14FR19	63-40 µm	Trachyte	70,15%
14FR01	100-63 µm	Basanite	67,99%	14FR03	40-0 µm	Basaltic trachyandesite	61,40%	14FR01	63-40 µm	Basanite	65,19%
14FR08	63-40 µm	Tephrite/basanite	67,52%	14FR19	40-0 µm	Trachyte	58,37%	14FR09	40-0 µm	Trachybasalt	60,77%
14FR14	40-0 µm	Trachybasalt	63,27%	14FR25	40-0 µm	Basalt	57,25%	14FR26	P.S.	Rhyolite	60,65%
14FR17	100-63 µm	Trachyte	63,16%	14FR26	H.S.	Rhyolite	54,91%	14FR26	160-100 µm	Rhyolite	60,35%
14FR08	40-0 µm	Tephrite/basanite	61,70%	14FR26	P.S.	Rhyolite	52,85%	14FR08	40-0 µm	Tephrite/basanite	57,90%
14FR17	160-100 µm	Trachyte	61,01%	14FR22	H.S.	Trachyte	52,83%	14FR27	160-100 µm	Trachyte	57,59%
14FR17	63-40 µm	Trachyte	59,66%	14FR18	63-40 µm	Phonolite	52,72%	14FR02	63-40 µm	Trachyandesite	56,01%
14FR22	40-0 µm	Trachyte	59,27%	14FR17	H.S.	Trachyte	50,89%	14FR19	100-63 µm	Trachyte	55,83%
14FR24	63-40 µm	Picrobasalt	58,57%	14FR17	P.S.	Trachyte	48,45%	14FR26	H.S.	Rhyolite	52,99%
14FR19	100-63 µm	Trachyte	58,38%	14FR14	63-40 µm	Trachybasalt	47,71%	14FR22	H.S.	Trachyte	52,14%
14FR18	100-63 µm	Phonolite	57,80%	14FR05	40-0 µm	Trachybasalt	47,65%	14FR02	100-63 µm	Trachyandesite	51,51%
14FR26	H.S.	Rhyolite	56,93%	14FR17	63-40 µm	Trachyte	47,56%	14FR17	63-40 µm	Trachyte	50,57%
14FR27	H.S.	Trachyte	51,08%	14FR22	P.S.	Trachyte	46,54%	14FR02	40-0 µm	Trachyandesite	50,56%
14FR09	63-40 µm	Trachybasalt	48,84%	14FR04	40-0 µm	Picrobasalt	46,48%	14FR26	100-63 µm	Rhyolite	50,21%
14FR22	63-40 µm	Trachyte	48,41%	14FR18	160-100 µm	Phonolite	46,27%	14FR09	63-40 µm	Trachybasalt	49,39%
14FR27	P.S.	Trachyte	48,05%	14FR19	63-40 µm	Trachyte	45,92%	14FR17	100-63 µm	Trachyte	49,18%
14FR26	160-100 µm	Rhyolite	47,86%	14FR17	40-0 µm	Trachyte	44,19%	14FR22	63-40 µm	Trachyte	48,53%
14FR11	40-0 µm	Trachybasalt	47,80%	14FR26	63-40 µm	Rhyolite	43,80%	14FR11	40-0 µm	Trachybasalt	48,45%

The studied powder (rock and grain size) is highlighted in orange; the other powders of the studied rock but with a different grain size are highlighted in pink.

Examples of matching results are displayed in Table 4 (results for all samples can be found in Table S2). For 32% of the powders the identification is exact, i.e., the studied powder corresponds to the highest matching value. The studied powder is in the top five for 91% of cases and in the top three for 59%. More interestingly, in 77% of cases, the best match occurs for the same rock but at a different grain size. Also in 77% of cases, the best match occurs for a sample with a similar grain size distribution (i.e., $40 \mu\text{m} > \text{G.S.} > 0 \mu\text{m}$). Finally, for 91% of cases, a rock with a similar or adjacent composition as defined by the TAS diagram is in the top three matches. This statistic is very high and demonstrates the efficiency of the method.

Similarly, the vector of the ESA-01-E microbasalt analogue sample (G.S. $< 40 \mu\text{m}$) was compared with the 132 vectors in the database. As displayed in Table 5 (see Table S2 for the complete table) the microbasalt (14FR04) with G.S. $< 40 \mu\text{m}$, i.e., a sample of similar rock type and grain size distribution, is the second best match. Interestingly, the match with this sample is very high (81.21%) and very close to the best match (82.01%). Moreover, it is also the only powder with a G.S. $< 40 \mu\text{m}$ and with a match higher than 70%, meaning that by estimating the grain size it would have been possible to identify the sample as demonstrated before (Table 3).

4. Discussion

4.1. TAS diagram versus CaliPhoto colours

We have demonstrated that, with the CaliPhoto method, it is possible to evaluate the composition of powdered rocks with a high degree of accuracy (Tables 2 and 3). In Fig. 8, the average RGB colours of the different powders studied are reported in the TAS diagram.

It was noted that the powders tend to be lighter with increasing content in silica, therefore, in order to confirm this phenomenon, pure quartz powder (Alfa Aesar, SiO₂ 99.5%, 2 μm APS) was added to the dataset and its luminance was plotted against silica content (Fig. 9), which showed that luminance increases more or less linearly with increasing silica content.

4.2. Grain size effects

It was shown that the apparent luminance of the powders varies with the grain size. The average RGB value of a powder thus does not permit the identification without knowing the grain size. On the other hand, using the colour vector, with the CaliPhoto method it is possible to identify the powder and to determine its grain size with a relatively good

accuracy. Nevertheless, here we only consider a limited set of samples. In order to free the analyses from grain size effects, it would thus be better to create the reference database with the drill fines of analogue samples prepared using similar drilling parameters to those used on Mars in order to obtain powders with a representative grain size distribution.

4.3. Coupling powders and hand samples

Fig. 5 shows that the change in colour between the uncrushed and the crushed samples varies from one rock to another; obsidian changes from black to light grey while basalts remain relatively dark. Since both the drilled outcrop and the associated drill fines on Mars, prepared using a Rock Abrasion Tool system for example, can be imaged, use the colour of the rock before and after crushing can improve its identification. New photographs of the polished samples were thus acquired under different illumination conditions (i.e., a change in the camera position and in the orientation and intensity of the light source). These new images of the polished samples, for which the names start by “UNK-”, are then considered as images of “unknown” samples to be identified by comparison with those of the database. They are displayed in Figs. S1 and S2 before and after CaliPhoto image processing, respectively. The average RGB values of the “unknown” polished samples were compared to those of the database using a matching parameter defined by Eq. (4), which was then combined with those obtained for the “unknown” powders according to the following matching parameter:

$$M_{ij} = M_{ij}^{Pol} \times M_{ij}^{Pow} \tag{7}$$

With M_{ij}^{Pol} and M_{ij}^{Pow} the matching values for polished and powdered (G.S. $< 40 \mu\text{m}$) samples, respectively. Examples of matching results are displayed in Table 6 (full results can be found in Table S3). The identification is exact for 68% of rocks, i.e., the studied powder corresponds to the highest matching identification from the database. In 95% of cases, the studied sample is in the top two matches, and in 100% of cases, it is in the top three. Moreover, when the studied sample is only in the second or third position, the difference with the best match is always lower than 1%. Considering 1% of uncertainty, it is thus possible to conclude that the identification is correct for all samples. This is all the more true since, in 82% of cases, the best match occurs for rocks with similar composition and, for 14% of cases, with a rock of adjacent composition as defined by the TAS diagram. The only rock for which the best match does not correspond to the studied rock nor to a rock with composition adjacent in the TAS diagram is the microbasalt 14FR24. Nevertheless, the best match occurs for the basaltic trachyandesite 14FR03 with a percent match of 93.97% while the sample 14FR24 is in second position with a percent match of 93.31%. The composition of these samples is also not very different (see Table 1 and Fig. 8). The interest of using the polished and powdered samples is the increase in the range of match percent (ranging between 99% and 30% against 99% and 60% with powders only). This strongly increases confidence in rock identification.

Similarly, the method was tested on powdered and polished section samples of the ESA analogue microbasalt (see Fig. 4). The combined RGB matching percentages, given by Eq. (7), against the samples of the reference database are given in Table 7, which demonstrates that the best match of 97.51% occurs with sample 14FR24 (microbasalt), and that the second match only 92.16%. The CaliPhoto method thus permits the clear identification of the ESA-01-E sample as a microbasalt.

5. Conclusions and perspectives

The CaliPhoto method was used to determine whether rock powders can be used to identify the composition of the parent rock and/or if their compositions can be estimated using only photographs. Using a diverse suite of volcanic rocks, we demonstrated that, for a given grain size

Table 5
Example of matching results for the unknown sample (ESA-01-E) against the average RGB values of the reference sample database (only the first 12 lines over 132; see Table S2 in supplementary materials for full results).

Database			ESA-01-E-40-0μm
			Picrobasalt
14FR19	63-40 μm	Trachyte	82,01%
14FR04	40-0 μm	Picrobasalt	81,21%
14FR18	160-100 μm	Phonolite	79,98%
14FR14	63-40 μm	Trachybasalt	78,96%
14FR19	100-63 μm	Trachyte	69,82%
14FR25	40-0 μm	Basalt	69,19%
14FR03	40-0 μm	Basaltic trachyandesite	67,04%
14FR05	40-0 μm	Trachybasalt	66,91%
14FR01	100-63 μm	Basanite	64,39%
14FR09	63-40 μm	Trachybasalt	63,64%
14FR08	63-40 μm	Tephrite/basanite	62,22%
14FR22	63-40 μm	Trachyte	61,63%

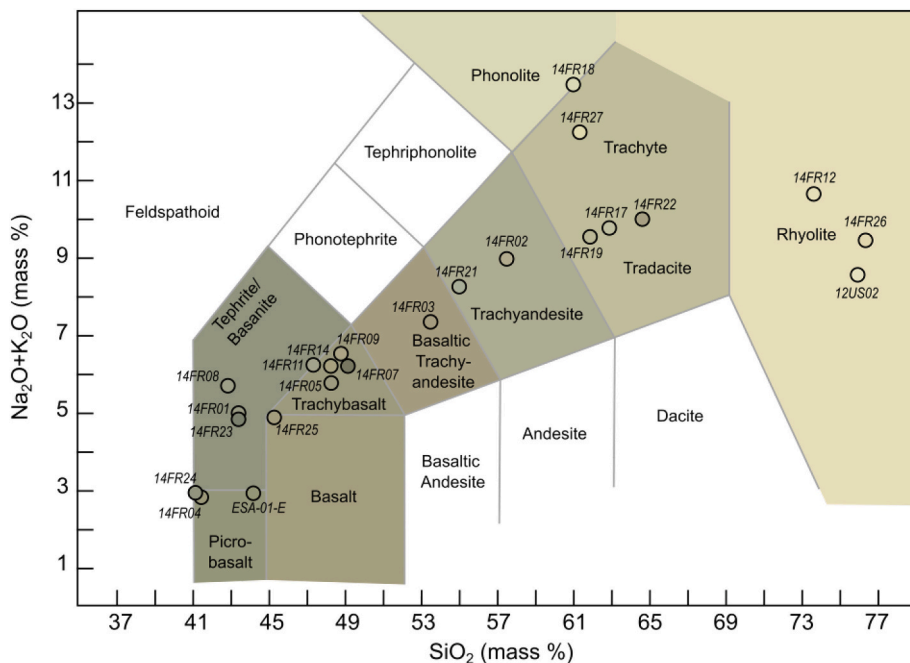


Fig. 8. TAS composition and average colour of the studied rock powders (grain size distribution <40 μm) after CaliPhoto image processing. The different domains of the TAS diagram are filled with the average colours of the corresponding powders.

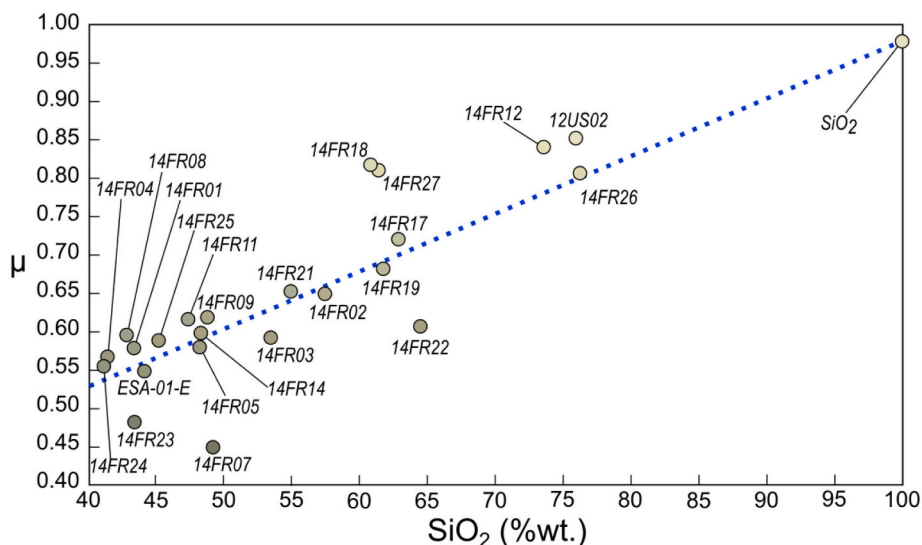


Fig. 9. Luminance versus SiO₂ content. Circles are filled with the average colour of the corresponding powdered samples (grain size distribution <40 μm) after CaliPhoto image processing.

distribution, it is possible to either identify a powder or estimate its composition using a reference database. For rocks included in the database created thus far, the method enables their identification with a very good level of accuracy. For rocks not included in the database, it was possible to make a good match based on rocks of similar composition in the database. Even for rocks having similar elemental composition but very different bulk colours, such as rhyolite (light) and obsidian (dark), the method permits accurate identification since they have a similar powder colour. Using various grain size distributions, we showed that the accuracy of identification remains good, permitting both the approximate grain size and the composition of the sample to be determined. Finally, by combining images of polished and crushed samples, it was possible to identify a rock in 70% of cases, 100% considering the uncertainties.

The CaliPhoto method is thus as a very useful tool for igneous rock identification. Of course, the method can still be improved. The number of rocks in the database can be increased to include other lithologies, sedimentary rocks in particular. Increasing the number of reference pictures per sample in the database would also improve the method. Similarly, using different images of the same powder could strongly improve its identification using a statistical approach (e.g., a Student's *t*-distribution or artificial intelligence/machine learning methods).

The CaliPhoto method could be very useful during planetary exploration to assist in the identification of rocks during drilling without requiring the addition of any new instrumentation, except a dedicated target. It uses compressed jpg images which, after resizing to 1200 × 1020 px, range from 600 to 1000 kilobytes. Moreover, it is possible to automatize target detection and implement the image-processing

Table 6

Examples of matches between the average RGB values of four samples (polished + powdered, G.S. < 40 µm) and those of the reference sample database.

Database		UNK-14FR01	Database		UNK-14FR02	Database		UNK-14FR03	Database		UNK-14FR04
		Basanite		Trachyandesite	Trachyandesite		Basaltic trachyandesite	Basaltic trachyandesite		Picrobasalt	Picrobasalt
14FR08	Tephrite/basanite	97,84%	14FR02	Trachyandesite	97,62%	14FR03	Basaltic trachyandesite	98,75%	14FR01	Basanite	98,06%
14FR01	Basanite	97,61%	14FR21	Trachyandesite	91,81%	14FR25	Basalt	97,23%	14FR04	Picrobasalt	97,92%
14FR04	Picrobasalt	95,65%	14FR19	Trachyte	90,54%	14FR02	Trachyandesite	93,44%	14FR08	Tephrite/basanite	96,44%
14FR05	Trachybasalt	93,92%	14FR03	Basaltic trachyandesite	90,49%	14FR01	Basanite	90,78%	14FR05	Trachybasalt	95,46%
14FR09	Trachybasalt	93,55%	14FR25	Basalt	90,29%	14FR08	Tephrite/basanite	89,67%	14FR09	Trachybasalt	93,37%
14FR11	Trachybasalt	92,15%	14FR09	Trachybasalt	83,91%	14FR09	Trachybasalt	89,59%	14FR25	Basalt	92,11%
14FR03	Basaltic trachyandesite	91,91%	14FR01	Basanite	83,11%	14FR04	Picrobasalt	89,46%	14FR03	Basaltic trachyandesite	91,89%
14FR25	Basalt	91,59%	14FR08	Tephrite/basanite	82,76%	14FR05	Trachybasalt	87,38%	14FR11	Trachybasalt	91,13%
14FR24	Picrobasalt	90,24%	14FR18	Phonolite	82,76%	14FR11	Trachybasalt	86,51%	14FR24	Picrobasalt	91,11%
14FR14	Trachybasalt	87,23%	14FR11	Trachybasalt	82,19%	14FR21	Trachyandesite	86,28%	14FR14	Trachybasalt	88,09%
14FR02	Trachyandesite	86,70%	14FR04	Picrobasalt	81,44%	14FR14	Trachybasalt	83,04%	14FR02	Trachyandesite	85,33%
14FR23	Basanite	82,54%	14FR05	Trachybasalt	79,65%	14FR24	Picrobasalt	82,85%	14FR23	Basanite	83,79%
14FR21	Trachyandesite	80,93%	14FR22	Trachyte	78,76%	14FR19	Trachyte	82,37%	14FR07	Trachybasalt	81,72%
14FR07	Trachybasalt	80,18%	14FR14	Trachybasalt	75,73%	14FR22	Trachyte	80,22%	14FR21	Trachyandesite	79,09%
14FR19	Trachyte	76,37%	14FR24	Picrobasalt	75,69%	14FR18	Phonolite	77,25%	14FR19	Trachyte	74,89%
14FR22	Trachyte	73,88%	14FR27	Trachyte	71,21%	14FR23	Basanite	75,87%	14FR22	Trachyte	73,36%
14FR18	Phonolite	72,36%	14FR23	Basanite	68,70%	14FR07	Trachybasalt	74,09%	14FR18	Phonolite	70,77%
14FR27	Trachyte	58,61%	14FR17	Trachyte	68,63%	14FR27	Trachyte	63,81%	14FR27	Trachyte	57,26%
12US02	Obsidian	56,99%	14FR07	Trachybasalt	66,73%	14FR17	Trachyte	61,60%	12US02	Obsidian	56,36%
14FR17	Trachyte	56,01%	14FR26	Rhyolite	64,15%	14FR26	Rhyolite	57,28%	14FR17	Trachyte	54,75%
14FR26	Rhyolite	52,04%	12US02	Obsidian	55,36%	12US02	Obsidian	53,77%	14FR26	Rhyolite	50,85%
14FR12	Rhyolite	42,55%	14FR12	Rhyolite	53,51%	14FR12	Rhyolite	47,27%	14FR12	Rhyolite	41,42%

These samples considered as “unknown” were imaged in different orientation and light conditions to those of the database. The results are given in percent match. (Full results are displayed in Supplementary Materials).

Table 7

Matches (in percent) of the average RGB values of the ESA-01-E with respect to those of the reference sample database (polished and powdered samples combined).

Database		ESA-01-E
		Picrobasalt
14FR24	Picrobasalt	97,51%
14FR23	Basanite	92,16%
14FR05	Trachybasalt	90,68%
14FR14	Trachybasalt	89,76%
14FR08	Tephrite/basanite	87,09%
14FR04	Picrobasalt	86,83%
14FR11	Trachybasalt	86,73%
14FR09	Trachybasalt	86,48%
14FR01	Basanite	85,13%
14FR07	Trachybasalt	84,59%
14FR03	Basaltic trachyandesite	78,53%
14FR25	Basalt	78,35%
14FR02	Trachyandesite	71,31%
14FR21	Trachyandesite	66,33%
12US02	Obsidian	65,15%
14FR19	Trachyte	61,83%
14FR18	Phonolite	60,65%
14FR22	Trachyte	57,62%
14FR27	Trachyte	45,23%
14FR17	Trachyte	42,15%
14FR26	Rhyolite	38,56%
14FR12	Rhyolite	31,91%

The highest matches occur for the picrobasalt 14FR24.

algorithm directly in the probe. In that case, only the average RGB values or colour vectors would be returned to Earth, totalling only a few tens of octets. Unfortunately, the reference target required for the CaliPhoto method will not be available during the ExoMars 2022 mission, and the calibration targets on board these rovers will never be located sufficiently close to the powders even to apply a simplified version of the method. It is nevertheless envisioned to try to use the method during ExoMars 2022 by using the model of the rover available on Earth. The idea is to reproduce in the laboratory the lightening conditions (light orientation, intensity and shadows) under which each photograph will be taken in situ, to make an image of the CaliPhoto reference target in these conditions, then to use this image to determine the CaliPhoto correction to apply to the photograph taken in situ, and finally to compare the processed images with those of an analogue sample database.

The CaliPhoto method is not intended to supplant more specific instrumentation, but rather to serve as a complementary method that could be more widely applied to the interpretation of data acquired using other techniques. Conversely, the identification of rock powders using the CaliPhoto method would be strongly improved by taking into account the geological context and complementary data obtained with other instruments.

Finally, CaliPhoto is a very low-cost method, easy to implement and to incorporate into any exploration protocols. It can be used to link optical images taken in the field using a standard camera to measurements obtained by laboratory instrumentation (ICP-AES data, for example). Its uses are thus not limited to space exploration, it could be readily applied to image-based studies in geology, materials science, biology, and other disciplines.

Author contributions

F. Foucher invented and developed the method, made the experiments and data processing, and wrote the article, N. Bost invented the method and wrote the article, G. Guimbretière invented the method and wrote the article, A. Courtois invented and developed the method, K. Hickman-Lewis developed the method and wrote the article, E. Marceau made the experiments, P. Martin developed the method and wrote the article and F. Westall developed the method and wrote the article.

Declaration of Competing Interest

The authors declare that they have no known competing financial interests or personal relationships that could have appeared to influence the work reported in this paper.

Acknowledgements

We acknowledge the *Maison du parc national des volcans d'Auvergne* for permission to sample. We thank CNRS, CNES and SATT Grand Centre for funding.

References

- Abbey, W., Anderson, R., Beegle, L., Hurowitz, J., Williford, K., Peters, G., Morookian, J. M., Collins, C., Feldman, J., Kinnett, R., Jandura, L., Limonadi, D., Logan, C., McCloskey, S., Melko, J., Okon, A., Robinson, M., Roumeliotis, C., Seybold, C., Singer, J., Warner, N., 2019. A look back: the drilling campaign of the curiosity rover during the Mars science laboratory's prime mission. *Icarus* 319, 1–13. <https://doi.org/10.1016/j.icarus.2018.09.004>.
- Abbey, W., Anderson, R., Beegle, L.W., Peters, G., Morookian, J.M., Biesiadecki, J., Carsten, J., Collins, C., Davis, K., Kinnett, R., Klein, D., Kuhn, S., Logan, C., Maimone, M., Melko, J., Okon, A., Reid, J., Robinson, M., Singer, J., Verma, V., Vasavada, A.R., 2020. A look back, part II: the drilling campaign of the curiosity rover during the Mars science laboratory's second and third martian years. *Icarus* 350, 113885. <https://doi.org/10.1016/j.icarus.2020.113885>.
- Adams, J.B., Filice, A.L., 1967. Spectral reflectance 0.4 to 2.0 microns of silicate rock powders. *J. Geophys. Res.* 72, 5705–5715.
- Bish, D.L., Blake, D.F., Vaniman, D.T., Chipera, S.J., Morris, R.V., Ming, D.W., Treiman, A.H., Sarrazin, P., Morrison, S.M., Downs, R.T., Achilles, C.N., Yen, A.S., Bristow, T.F., Crisp, J.A., Morookian, J.M., Farmer, J.D., Rampe, E.B., Stolper, E.M., Spanovich, N., Team, M.S., 2013. X-ray diffraction results from Mars science laboratory: mineralogy of rocknest at gale crater. *Science* 341, 1238932–(1–5).
- Blake, D.F., Morris, R.V., Kocurek, G., Morrison, S.M., Downs, R.T., Bish, D., Ming, D.W., Edgett, K.S., Rubin, D., Goetz, W., Madsen, M.B., Sullivan, R., Gellert, R., Campbell, I., Treiman, A.H., McLennan, S.M., Yen, A.S., Grotzinger, J., Vaniman, D. T., Chipera, S.J., Achilles, C.N., Rampe, E.B., Sumner, D., Meslin, P.-Y., Maurice, S., Forni, O., Gasnault, O., Fisk, M., Schmidt, M., Mahaffy, P., Leshin, L.A., Glavin, D., Steele, A., Freissinet, C., Navarro-Gonzalez, R., Yingst, R.A., Kah, L.C., Bridges, N., Lewis, K.W., Bristow, T.F., Farmer, J.D., Crisp, J.A., Stolper, E.M., Marais, D.J.D., Sarrazin, P., Team, M.S., 2013. Curiosity at gale crater, Mars: characterization and analysis of the rocknest sand shadow. *Science* 341, 1239505–(1–7).
- Bost, N., Westall, F., Ramboz, C., Foucher, F., Pullan, D., Meunier, A., Petit, S., Fleischer, I., Klingelhöfer, G., Vago, J., 2013. Missions to Mars: characterisation of Mars analogue rocks for the International Space Analogue Rockstore (ISAR). *Planet. Space Sci.* 82–83, 113–127.
- Coates, A.J., Jaumann, R., Griffiths, A.D., Leff, C.E., Schmitz, N., Josset, J.-L., Paar, G., Gunn, M., Hauber, E., Cousins, C.R., Cross, R.E., Grindrod, P., Bridges, J.C., Balme, M., Gupta, S., Crawford, I.A., Irwin, P., Stabbins, R., Tirsch, D., Vago, J.L., Theodorou, T., Caballo-Perucha, M., Osinski, G.R., the PanCam Team, 2017. The PanCam instrument for the ExoMars rover. *Astrobiology* 17, 511–541. <https://doi.org/10.1089/ast.2016.1548>.
- Cousins, C.R., Gunn, M., Prosser, B.J., Barnes, D.P., Crawford, I.A., Griffiths, A.D., Davis, L.E., Coates, A.J., 2012. Selecting the geology filter wavelengths for the ExoMars Panoramic Camera instrument. *Planet. Space Sci.* 71, 80–100.
- Farley, K.A., Williford, K.H., Stack, K.M., Bhartia, R., Chen, A., de la Torre, M., Hand, K., Goreva, Y., Herd, C.D.K., Hueso, R., Liu, Y., Maki, J.N., Martinez, G., Moeller, R.C., Nelessen, A., Newman, C.E., Nunes, D., Ponce, A., Spanovich, N., Willis, P.A., Beegle, L.W., Bell, J.F., Brown, A.J., Hamran, S.-E., Hurowitz, J.A., Maurice, S., Paige, D.A., Rodriguez-Manfredi, J.A., Schulte, M., Wiens, R.C., 2020. Mars 2020 mission overview. *Space Sci. Rev.* 216, 142. <https://doi.org/10.1007/s11214-020-00762-y>.
- Foucher, Guimbretière, Bost, Hickman-Lewis, Courtois, Luengo, Marceau, Bergouiniou, Westall, 2019. The CaliPhoto method. *Inventions* 4, 67. <https://doi.org/10.3390/inventions4040067>.
- Goetz, W., Pike, W.T., Hviid, S.F., Madsen, M.B., Morris, R.V., Hecht, M.H., Stauffer, U., Leer, K., Sykulska, H., Hemmig, E., Marshall, J., Morookian, J.M., Parrat, D., Vijendran, S., Bos, B.J., Maarry, M.R.E., Keller, H.U., Kramm, R., Markiewicz, W.J., Drube, L., Blaney, D., Arvidson, R.E., Bell III, J.F., Reynolds, R., Smith, P.H.,

- Woida, P., Woida, R., Tanner, R., 2010. Microscopy analysis of soils at the Phoenix landing site, Mars: classification of soil particles and description of their optical and magnetic properties. *J. Geophys. Res.* 115, E00E22.
- Grott, M., Knollenberg, J., Hamm, M., Ogawa, K., Jaumann, R., Otto, K.A., Delbo, M., Michel, P., Biele, J., Neumann, W., Knappmeyer, M., Kühr, E., Senshu, H., Okada, T., Helbert, J., Maturilli, A., Müller, N., Hagermann, A., Sakatani, N., Tanaka, S., Arai, T., Mottola, S., Tachibana, S., Pelivan, I., Drube, L., Vincent, J.-B., Yano, H., Pilorget, C., Matz, K.D., Schmitz, N., Koncz, A., Schröder, S.E., Trauthan, F., Schlotterer, M., Krause, C., Ho, T.-M., Moussi-Soffys, A., 2019. Low thermal conductivity boulder with high porosity identified on C-type asteroid (162173) Ryugu. *Nat. Astron.* 3, 971–976. <https://doi.org/10.1038/s41550-019-0832-x>.
- Grotzinger, J.P., Crisp, J., Vasavada, A.R., Anderson, R.C., Baker, C.J., Barry, R., Blake, D.F., Conrad, P., Edgett, K.S., Ferdowski, B., Gellert, R., Gilbert, J.B., Golombek, M., Gomez-Elvira, J., Hassler, D.M., Jandura, L., Litvak, M., Mahaffy, P., Maki, J., Meyer, M., Malin, M.C., Mitrofanov, I., Simmonds, J.J., Vaniman, D., Welch, R.V., Wiens, R.C., 2012. Mars science laboratory mission and science investigation. *Space Sci. Rev.* 170, 5–56.
- Hazeli, K., El Mir, C., Papanikolaou, S., Delbo, M., Ramesh, K.T., 2018. The origins of Asteroidal rock disaggregation: interplay of thermal fatigue and microstructure. *Icarus* 304, 172–182. <https://doi.org/10.1016/j.icarus.2017.12.035>.
- Horgan, B.H.N., Anderson, R.B., Dromart, G., Amador, E.S., Rice, M.S., 2020. The mineral diversity of Jezero crater: evidence for possible lacustrine carbonates on Mars. *Icarus* 339, 113526. <https://doi.org/10.1016/j.icarus.2019.113526>.
- Iñigo, A.C., Garcia-Talegon, J., Vicente-Tavera, S., Martin-Gonzalez, S., Casado-Marin, S., Vargas-Muñoz, M., Pérez-Rodríguez, J.L., 2013. Colour and ultrasound propagation speed changes by different ageing of freezing/thawing and cooling/heating in granitic materials. *Cold Reg. Sci. Technol.* 85, 71–78.
- Johnson, J.R., Bell, J.F., Bender, S., Blaney, D., Cloutis, E., Ehlmann, B., Fraeman, A., Gasnault, O., Kinch, K., Le Mouélic, S., Maurice, S., Rampe, E., Vaniman, D., Wiens, R.C., 2016. Constraints on iron sulfate and iron oxide mineralogy from ChemCam visible/near-infrared reflectance spectroscopy of Mt. Sharp basal units, Gale Crater, Mars. *Am. Mineral.* 101, 1501–1514. <https://doi.org/10.2138/am-2016-5553>.
- Josset, J.-L., Westall, F., Hofmann, B.A., Spray, J., Cockell, C., Kempe, S., Griffiths, A.D., Sanctis, M.C.D., Colangeli, L., Koschny, D., Föllmi, K., Verrecchia, E., Diamond, L., Josset, M., Javaux, E.J., Esposito, F., Gunn, M., Souchon-Leitner, A.L., Bontognali, T. R.R., Korabiev, O., Erkman, S., Paar, G., Ulamec, S., Foucher, F., Martin, P., Verhaeghe, A., Tanevski, M., Vago, J.L., 2017. The close-up imager onboard the ESA ExoMars rover: objectives, description, operations, and science validation activities. *Astrobiology* 17, 595–611.
- Kempe, D.B., 2014. Colorimetric characterisation of flatbed scanners for rock/sediment imaging. *Comput. Geosci.* 67, 69–74.
- Martin, D.J.P., Duvet, L., 2019. ESA's Sample Analogue Curation Facility (SACF), and Expanding ESA's Exploration Sample Analogue Collection (ESA2C). In: LPI Contrib. No. 2132. Presented at the 50th Lunar and Planetary Science Conference, 2663.
- McCamy, C.S., Marcus, H., Davidson, J.G., 1976. A color-rendition chart. *J. Appl. Photogr. Eng.* 2, 95–99.
- McSween, H.Y., Taylor, G.J., Wyatt, M.B., 2009. Elemental composition of the Martian crust. *Science* 324, 736–739.
- Meslin, P.-Y., Gasnault, O., Forni, O., Schröder, S., Cousin, A., Berger, G., Clegg, S.M., Lasue, J., Maurice, S., Sautter, V., Mouélic, S.L., Wiens, R.C., Fabre, C., Goetz, W., Bish, D., Mangold, N., Ehlmann, B., Lanza, N., Harri, A.-M., Anderson, R., Rampe, E., McConnochie, T.H., Pinet, P., Blaney, D., Léveillé, R., Archer, D., Barraclough, B., Bender, S., Blake, D., Blank, J.G., Bridges, N., Clark, B.C., DeFlores, L., Delapp, D., Dromart, G., Dyar, M.D., Fisk, M., Gondet, B., Grotzinger, J., Herkenhoff, K., Johnson, J., Lacour, J.-L., Langevin, Y., Leshin, L., Lewin, E., Madsen, M.B., Melikechi, N., Mezzacappa, A., Mischna, M.A., Moores, J.E., Newsom, H., Ollila, A., Perez, R., Renno, N., Sirven, J.-B., Tokar, R., de la Torre, M., d'Uston, L., Vaniman, D., Yingst, A., MSL-Science-Team, 2013. Soil diversity and hydration as observed by ChemCam at Gale Crater. *Mar. Sci.* 341 (1238670), 10.
- Oestmo, S., 2013. Digital imaging technology and experimental archeology: a methodological framework for the identification and interpretation of fire modified rock (FMR). *J. Archaeol. Sci.* 40, 4429–4443.
- Pascale, D., 2016. RGB Coordinates of the Macbeth ColorChecker.
- Quantin-Nataf, C., Carter, J., Mandon, L., Tholot, P., Balme, M., Volat, M., Pan, L., Loizeau, D., Millot, C., Breton, S., Dehouck, E., Fawdon, P., Gupta, S., Davis, J., Grindrod, P.M., Pacifici, A., Bultel, B., Allemand, P., Ody, A., Lozach, L., Broyer, J., 2021. Oxia planum: the landing site for the ExoMars "Rosaling Franklin" Rover Mission: geological context and prelanding interpretation. *Astrobiology*. <https://doi.org/10.1089/ast.2019.2191>.
- Smith, C.L., Gill, S.-J., Manick, K., Miller, C.G., Jones, C., Rumsey, M.S., Duvet, L., 2018. The European Space Agency exploration sample analogue collection (ESA2C) and curation facility – present and future. In: LPI Contrib. No. 2083. Presented at the 49th Lunar and Planetary Science Conference, p. 1623.
- Squyres, S.W., Arvidson, R.E., Bell III, J.F., Brückner, J., Cabrol, N.A., Calvin, W., Carr, M.H., Christensen, P.R., Clark, B.C., Crumpler, L., des Marais, D.J., d'Uston, C., Economou, T., Farmer, J., Farrand, W., Folkner, W., Golombek, M., Gorevan, S., Grant, J.A., Greeley, R., Grotzinger, J.P., Haskin, L., Herkenhoff, K.E., Hviid, S., Johnson, J., Klingelhöfer, G., Knoll, A.H., Landis, G., Lemmon, M., Li, R., Madsen, M. B., Malin, M.C., McLennan, S.M., McSween, H.Y., Ming, D.W., Moersch, J., Morris, R. V., Parker, T., Rice Jr., J.W., Richter, L., Rieder, R., Sims, M., Smith, M., Smith, P., Soderblom, L.A., Sullivan, R., Wänke, H., Wdowiak, T., Wolff, M., Yen, A., 2004. The Spirit Rover's Athena science investigation at Gusev Crater, Mars. *Science* 305, 794–799.
- Turkevich, A.L., 1973. The average chemical composition of the lunar surface. *Geochim. Cosmochim. Acta Proc. Fourth Lunar Sci. Conf.* 2, 1159–1168.
- Vago, J.L., Westall, F., Teams, Pasteur Instrument, Landing, S., Coates, A.J., Jaumann, R., Korabiev, O., Ciarletti, V., Mitrofanov, I., Josset, J.-L., De Sanctis, M.C., Bibring, J.-P., Rull, F., Goesmann, F., Steininger, H., Goetz, W., Brinckerhoff, W., Szopa, C., Raulin, F., Westall, F., Edwards, H.G.M., Whyte, L.G., Fairén, A.G., Bibring, J.-P., Bridges, J., Hauber, E., Ori, G.G., Werner, S., Loizeau, D., Kuzmin, R.O., Williams, R. M.E., Flahaut, J., Forget, F., Vago, J.L., Rodionov, D., Korabiev, O., Svedhem, H., Sefton-Nash, E., Kminek, G., Lorenzoni, L., Joudrier, L., Mikhailov, V., Zashchirinskiy, A., Alexashkin, S., Calantropio, F., Merlo, A., Poulakis, P., Witasse, O., Bayle, O., Bayón, S., Meierhenrich, U., Carter, J., García-Ruiz, J.M., Baglioni, P., Haldemann, A., Ball, A.J., Debus, A., Lindner, R., Haessig, F., Monteiro, D., Trautner, R., Volland, C., Rebeyle, P., Goult, D., Didot, F., Durrant, S., Zekri, E., Koschny, D., Toni, A., Visentin, G., Zwick, M., van Winnendael, M., Azkarate, M., Carreau, C., the ExoMars Project Team, 2017. Habitability on early Mars and the search for biosignatures with the ExoMars Rover. *Astrobiology* 17, 471–510. <https://doi.org/10.1089/ast.2016.1533>.
- Wellington, D.F., Bell, J.F., Johnson, J.R., Kinch, K.M., Rice, M.S., Godber, A., Ehlmann, B.L., Fraeman, A.A., Hardgrove, C., the MSL Science Team, 2017. Visible to near-infrared MSL/Mastcam multispectral imaging: initial results from select high-interest science targets within Gale Crater, Mars. *Am. Mineral.* 102, 1202–1217. <https://doi.org/10.2138/am-2017-5760CCBY>.